Journal of Molecular Modeling (2023) 29:205
https://doi.org/10.1007/s00894-023-05580-x

ORIGINAL PAPER

On the structural, electronic, and optical properties of L-histidine crystal: a DFT study

F. A. R. Pereira[1] · A. Macedo-Filho[1,2] · A. M. Silva[3] · N. F. Frazão[4] · R. G. Sarmento[5] · K. A. L. Lima[1] · J. J. S. Melo[6] · M. L. Pereira Junior[7] · L. A. Ribeiro Junior[8] · V. N. Freire[9]

Received: 24 March 2023 / Accepted: 3 May 2023 / Published online: 9 June 2023

Abstract

Context The monoclinic L-histidine crystal is critical for protein structure and function and is also found in the myelin of brain nerve cells. This study numerically examines its structural, electronic, and optical properties. Our findings indicate that the L-histidine crystal has an insulating band gap of approximately 4.38 eV. Additionally, electron and hole effective masses range between $3.92m_0$–$15.33m_0$ and $4.16m_0$–$7.53m_0$, respectively. Furthermore, our investigation suggests that the L-histidine crystal is an excellent UV collector due to its strong optical absorption activity for photon energies exceeding 3.5 eV.

Methods To investigate the structural, electronic, and optical properties of L-histidine crystals, we used the Biovia Materials Studio software to conduct Density Functional Theory (DFT) simulations as implemented in the CASTEP code. Our DFT calculations were performed using the generalized gradient approximation (GGA) as parameterized by the Perdew-Burke-Ernzerhof (PBE) exchange-correlation functional, with an additional dispersion energy correction (PBE + TS) based on the model proposed by Tkatchenko and Scheffler to describe van der Waals interactions. Additionally, we employed the norm-conserving pseudopotential to treat core electrons.

Keywords L-Histidine crystal · Electronic structure · Optical properties · Structural properties · DFT calculations

Introduction

Histidine is an essential amino acid with an imidazole functional group in its side chain, giving it aromatic properties [49]. It is one of the twenty standard amino acids found in proteins in all living organisms, existing in both D-histidine and L-histidine isomeric forms [50]. This amino acid plays a significant role in various biological mechanisms, including the formation of hemoglobin [51], and is also used to treat conditions such as allergic diseases and anemia [1–4].

One critical feature of Histidine is that it's the only amino acid whose side chain can shift from a non-protonated to a protonated state, allowing it to exhibit both acid and nucleophilic functionality [52]. The non-protonated state plays a crucial role as a base for the conformational stability of proteins [1, 5]. Additionally, the structural stability of amino acid crystals is currently an active area of research, as these structures have the potential for application in technological devices [3].

L-Histidine is a noteworthy amino acid as the human body cannot synthesize it and must be obtained through diet [7–9]. It plays a crucial role in many biological functions, such as the development and maintenance of myelin, which is responsible for communication between the brain and body, as well as the regulation of essential metal levels like zinc, iron, copper, and nickel [10]. L-Histidine has many applications, including biosynthesis [1, 4], metabolism, physiological importance, and supplementation [11]. It is also involved in human genome transcription factors [12], L-histidine capped Ag and Au nanoparticles for dopamine detection [13], and protein interactions [14].

Recently, L-histidine has attracted significant interest for both experimental and theoretical researchers [53–59]. Monocrystalline samples of L-histidine hydrochloride monohydrate were analyzed using Raman spectroscopy to

This paper belongs to the Topical Collection IX Symposium on Electronic Structure and Molecular Dynamics - IX SeedMol.

✉ M. L. Pereira Junior
marcelo.lopes@unb.br

Extended author information available on the last page of the article

investigate the effect of temperature changes on the vibrational spectrum [3]. Y. Wang and colleagues developed a straightforward, non-destructive method using terahertz frequency-domain spectroscopy to quickly and accurately analyze L-histidine and α-lactose in dietary supplements [6]. Their findings demonstrated high accuracy levels ranging from 94.8 to 110% for L-histidine and 98.9 to 110% for α-lactose, comparable to those of ion chromatography and high-performance liquid chromatography, respectively [6]. These results highlight the potential of the developed method for rapid, in situ analysis of nutrients in dietary supplements.

To compare theoretical and experimental results, terahertz spectroscopy and density functional theory (DFT) calculations were used to analyze the low-frequency vibration of pure solid-state L-histidine crystals, and their monohydrochloride monohydrate [15]. Results showed notable differences in the contribution of intermolecular movement and the distortions of the dihedral angle of the imidazole ring between the crystals. In another study, the spectroscopic properties of the stable semi-organic complex L-histidine tetrafluoroborate were also investigated [16]. It was demonstrated that Infra-Red and Raman spectroscopy's experimental and DFT calculation data agree well. The findings also indicated that L-histidine tetrafluoroborate is a stable complex suitable as a new violet-light emitting material with high non-linear properties and potential applications as an efficient optical limiter.

Previous studies have shown that molecules and crystals from the L-histidine family exhibit non-linear optical effects due to the presence of the imidazole ring [16–22]. This property is common to other amino acid crystals [23–28], suggesting that these structures are potential candidates for second harmonic generators, frequency converters, light modulators, optical commutators, and optical memory storage applications. The unique features and significant role of L-histidine crystals discussed earlier suggest that a comprehensive investigation into their properties could pave the way for their use in diverse optoelectronic applications.

The present study used DFT calculations to investigate L-histidine crystals' structural, electronic, and optical properties. Our findings suggest that the crystal has an insulating band gap of approximately 4.38 eV, with electron and hole effective masses ranging between $3.92m_0$–$15.33m_0$ and $4.16m_0$–$7.53m_0$, respectively. Our investigation also suggests that L-histidine crystals are excellent UV collectors, displaying strong optical absorption for photon energies exceeding 3.5 eV. This paper is organized as follows: the "Methodology" section describes the computational approach used to obtain the properties of interest, while "Structural properties", "Electronic properties", and "Optical properties" sections discuss the results for the structural, electronic, and optical properties of model L-histidine crystals. Finally, the "Conclusions" section presents the concluding remarks.

Methodology

The monoclinic form of the L-histidine crystal, with a chemical formula of $C_6H_9N_4O_2$, was studied. This amino acid is composed of four functional groups: carboxyl (COO^-), amino ($NH3^+$), imidazole ring ($C_3N_2H_3$), and lateral chain ($C5N2H_7$), as illustrated in Fig. 1a). The unit cell of the monoclinic L-histidine (mLH) crystal, consisting of two molecules and their respective hydrogen bonds, is shown in Fig. 1b). In Fig. 1c), a ($3 \times 1 \times 3$) L-histidine crystal supercell is displayed. The Biovia Materials Studio software was used to conduct DFT simulations as implemented in the CASTEP code [36, 37]. We used the generalized gradient approximation (GGA) as parameterized by the Perdew-Burke-Ernzerhof (PBE) exchange-correlation functional [35], with an additional dispersion energy correction (PBE + TS) based on the model proposed by Tkatchenko and Scheffler [39] to describe van der Waals interactions. We employed norm-conserving pseudopotentials to treat core electrons [41].

Experimental data indicate that the mLH crystal forms four distinct hydrogen bonds: N3-H$\cdots$O1 (at $x, y, -1+z$), N1-H$\cdots$O2 (at $-1+x, y, z$), N1-H$\cdots$O2 (at $1-x, \frac{1}{2}+y, -1+z$), and N1-H$\cdots$N2 (intramolecular) [40]. The molecule's conformation is stabilized by the intramolecular hydrogen bond between N1-H$\cdots$N2 [40].

The unit cell of the mLH crystal was geometrically optimized using the following set of converge criteria for the self-consistent field (SCF) calculations: SCF tolerance of 5×10^{-6} eV/atom, a maximum force on each atom of 0.01 eV/Å, pressure limit of 0.01 GPa, and maximum atomic displacement of 5×10^{-4} Å, and cutoff energy of about 830 eV. To optimize the unit cell, we employed the BFGS (Broyden, Fletcher, Goldfarb, and Shanno) algorithm [42]. The tolerance for each SCF step was tested to achieve convergence, ensuring that the total/atom energy variation is approximately 5×10^{-7} eV/atom and the eigenvalues are less than 3.33×10^{-7} eV for three successive steps.

Results

Structural properties

The mLH crystal, as classified by X-ray experimental data, belongs to the spatial group $P2_1$ and has the following crystal parameters (refer to Fig. 1): **a**=5.17 Å, **b**=7.38 Å, **c**=9.49 Å, $\beta = 97.16°$, and **V**=359.00 Å^3 [40]. Our theoretical calculations, which are in good agreement with the experimental

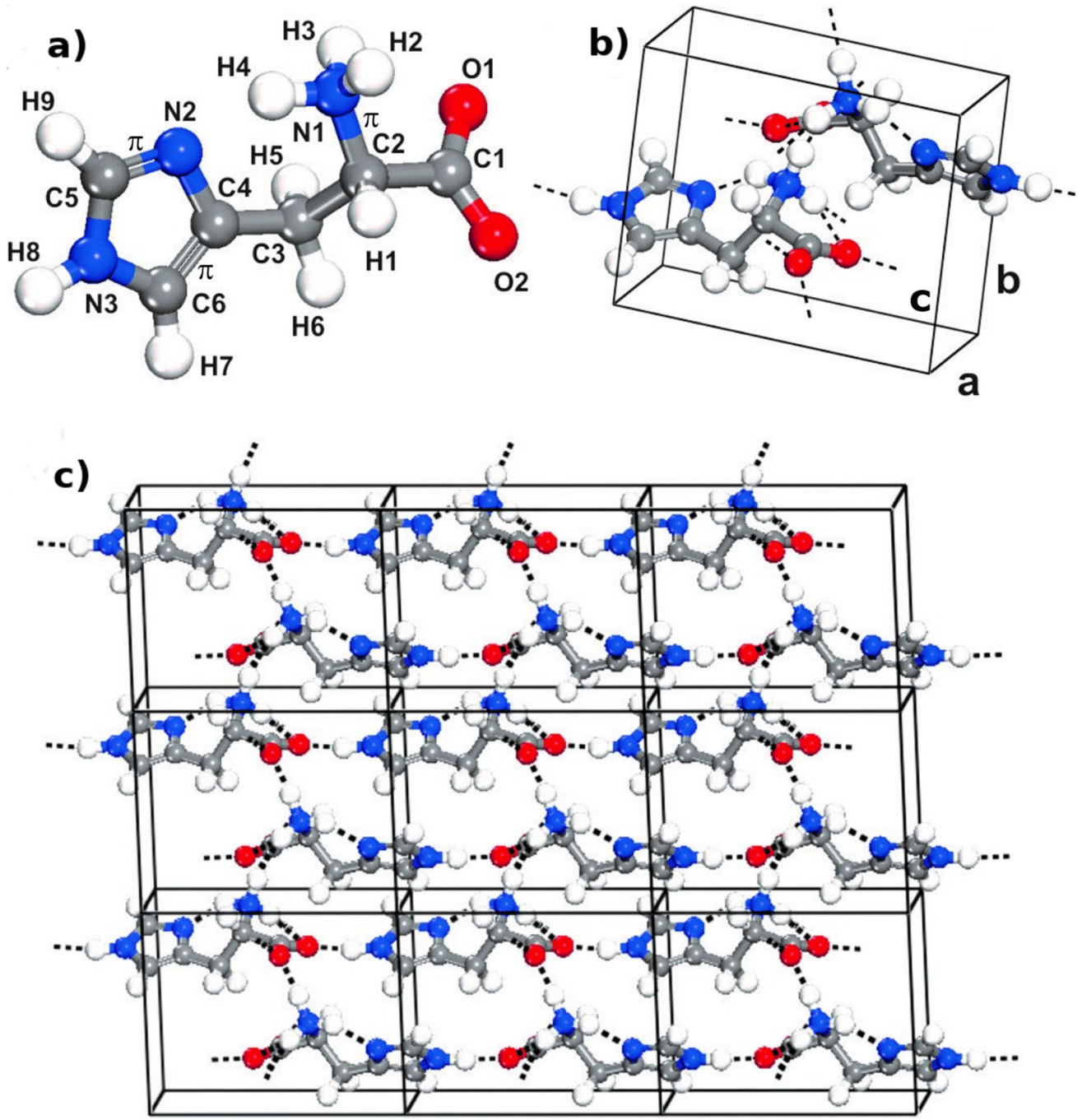

Fig. 1 Panel (a) depicts the schematic representation of the LH molecule with its constituent atoms represented as follows: oxygen (red), nitrogen (blue), carbon (gray), and hydrogen (white). Panel (b) displays the unit cell of the mLH crystal, while panel (c) shows a $(3 \times 1 \times 3)$ mLH crystal supercell, where the hydrogen bonds are highlighted

data, yielded: **a**=5.13 Å, **b**=7.36 Å, **c**=9.47 Å $\beta = 97.76°$, **V**=354.80 Å^3.

When comparing the atomic positions obtained from our theoretical calculations to experimental data, we found that the x-coordinate of H1 bonded to C2 had the largest deviation, with $\Delta x = -0.091$ Å. The y- and z-coordinates of the H2 and H4 hydrogen atoms bonded to N1 also showed deviations, with $\Delta y = -0.068$ Å and $\Delta z = -0.049$ Å, respectively. We observed deviations in the theoretical hydrogen bond lengths, with the C1-C2 bond having the largest relative deviation at about 23.323%, while the others did not exceed 3.624%. Additionally, we obtained a relative deviation of about 7.4%

in the angle of the C3-C4-N2 bond compared to experimental data, which is the largest one. These results suggest that our approach accurately reproduces the structural parameters reported in the experiment [40] and is suitable for analyzing mLH crystals' electronic and optical properties.

Electronic properties

We now discuss the electronic properties of the mLH crystal. Table 1 shows the electrical charge per atom, and functional group, distributions in the L-histidine molecule obtained from Mulliken's and Hirshfeld's electronic population analysis [43–45]. The results are expressed in elementary charge unit e. Our analysis reveals that the C1 has the highest positive charge, with Mulliken's (Hirshfield's) charges of about $0.66e$ ($0.16e$), while the N1 has the highest negative charge, with Mulliken's (Hirshfield's) charges of about $-0.77e$ ($-0.07e$).

Table 2 presents Mulliken's and Hirshfeld's electronic population for the carboxyl (COO^-), amino, imidazole ring, and lateral chain functional groups. The corresponding Mulliken's (Hirshfield's) charges are about $-0.67e$ ($-0.31e$), $0.09e$ ($0.06e$), $0.23e$ ($0.10e$), and $1.59e$ ($0.23e$), respectively. These findings indicate a dipolar behavior of the zwitterionic state inside the crystal [45–47]. It is worth noting that the zwitterionic structure of L-histidine holds, even in the gas phase, as reported in references [60, 61]. As a result, the atomic charge configuration tends to be also similar.

Table 1 Mulliken and Hirshfeld electronic population analysis of mLH crystal

Atoms	Mulliken	Rirshfeld
H1	+0.28	+0.04
H2	+0.29	+0.04
H3	+0.27	+0.04
H4	+0.30	+0.05
H5	+0.28	+0.04
H6	+0.43	+0.10
H7	+0.41	+0.10
H8	+0.43	+0.10
H9	+0.43	+0.10
C1	+0.66	+0.16
C2	−0.15	+0.02
C3	−0.52	−0.07
C4	+0.08	+0.01
C5	+0.06	+0.04
C6	−0.16	−0.03
N1	−0.77	−0.07
N2	−0.51	−0.16
N3	−0.51	−0.06
O1	−0.66	−0.24
O2	−0.67	−0.23

Table 2 Mulliken and Hirshfeld electronic population analysis of carboxyl, amino, imidazole ring and lateral chain functional group

Atoms	Mulliken	Rirshfeld
Carboxyl	−0.67	−0.31
Amino	+0.09	+0.06
Imidazole ring	+0.23	+0.10
Lateral chain	+1.59	+0.23

Figure 2 illustrates the high symmetric k-point path in the first Brillouin zone. The high-symmetry k-points are Γ (0,0,0), Z (0,0,1/2), Y (0,1/2,0), A (-1/2,1/2,0), B (-1/2,0,0), C (0,1/2,1/2), D (-1/2,0,1/2), and E (-1/2,1/2,1/2).

The band structure configuration and the corresponding total density of states (DOS) of mLH are shown in Fig. 3. The top panels, i.e., Fig. 3a), b), and c), provide an overview

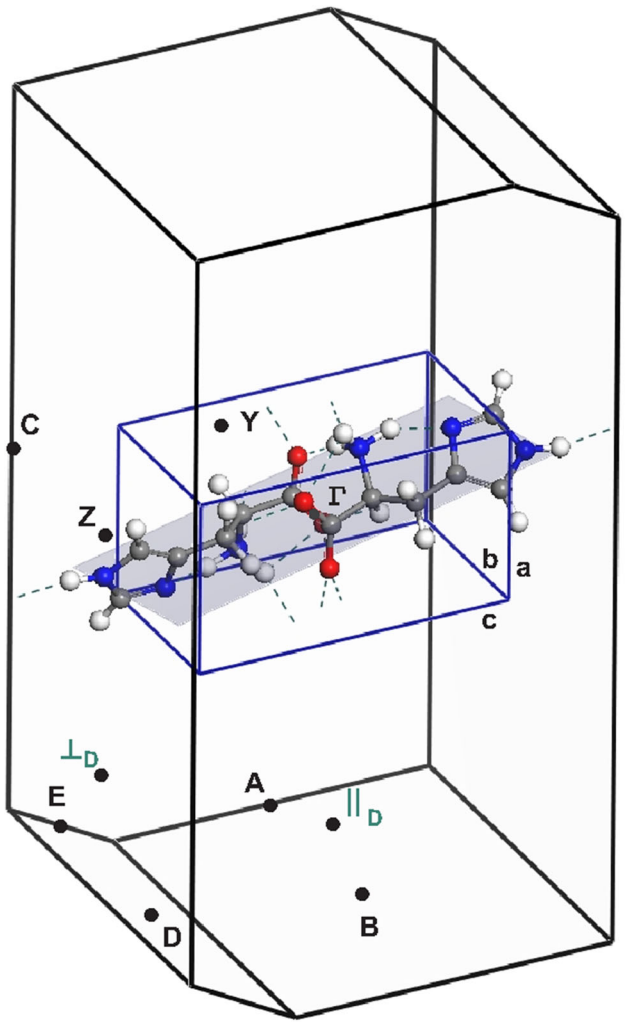

Fig. 2 The first Brillouin zone of the mLH crystal, including the high-symmetry k-points of the reciprocal lattice (designated with capital letters)

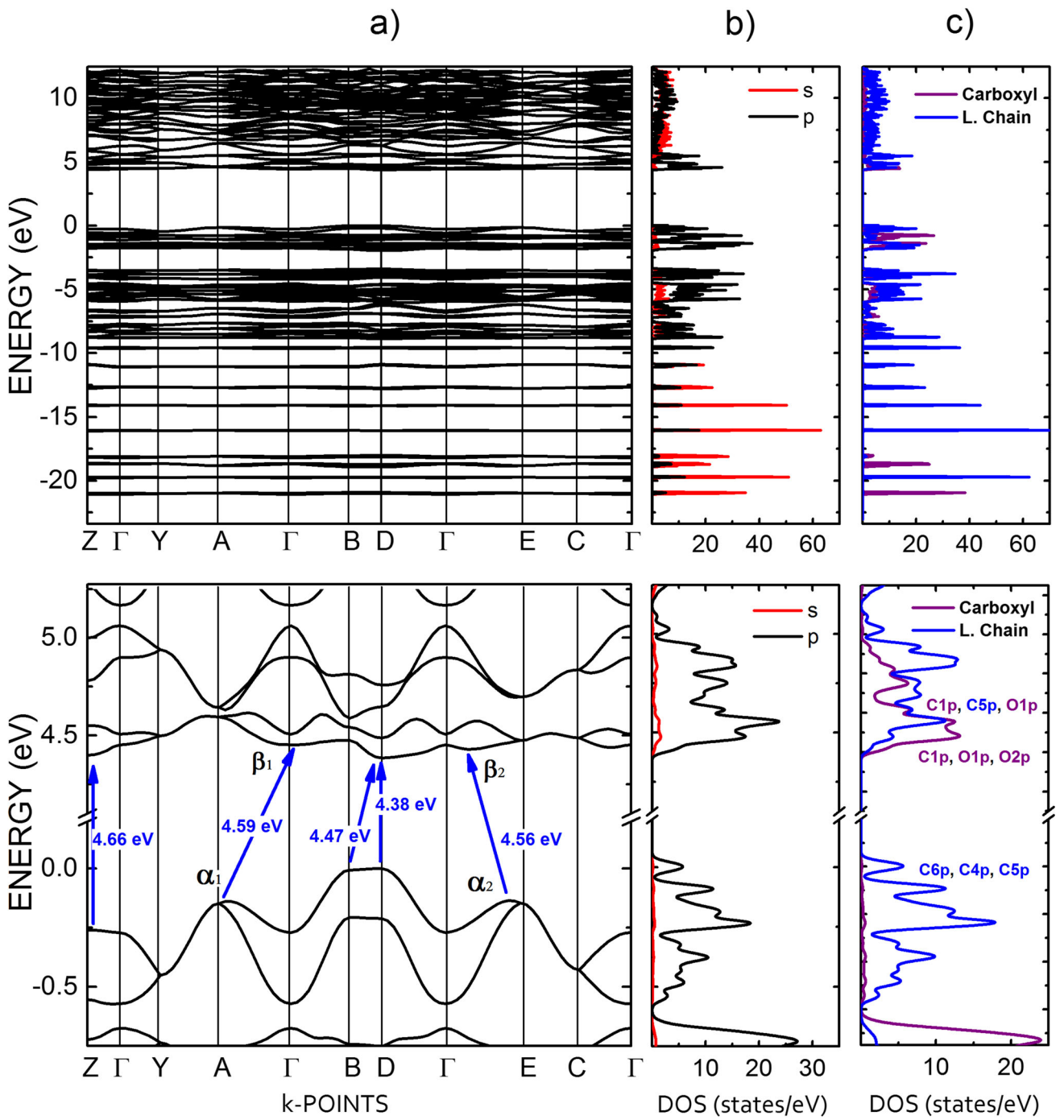

Fig. 3 Band structure configuration, and related total density of states (DOS), of mLH. Panels a), b), and c) depict the full bandgap structure, the DOS for the mLH crystal, and the DOS for the carboxyl and lateral chain functional groups, respectively. The bottom panels offer a closer look at these quantities for energies ranging from −0.7 eV to 5.2 eV. The energy levels were shifted according to the Fermi level

of the full bandgap structure, the DOS for the mLH crystal, and the DOS for the carboxyl and lateral chain functional groups, respectively. The bottom panels offer a closer look at these quantities for energies ranging from −0.7 eV to 5.2 eV, with the energy levels shifted relative to the Fermi level. Notably, the mLH crystal exhibits an insulating direct band gap of approximately 4.38 eV along the $D \rightarrow D$ path. Other possible indirect electron transfer channels include the $B \rightarrow D$ (4.47 eV), $A \rightarrow \Gamma$ (4.59 eV, labeled as $\alpha_1 \rightarrow \beta_1$), $E \rightarrow \Gamma$ (4.56 eV, labeled as $\alpha_2 \rightarrow \beta_2$), and $Z \rightarrow Z$ (4.66 eV) paths.

Figure 3b) (top panel) shows that in the lowermost valence band, the s orbital dominates, while s and p orbitals contribute to form the uppermost level of the conduction band. In Fig. 3b) (bottom panel), we see that the p orbitals are prominent at the top of the valence band as well as in the lowermost energy levels of the conduction band. Lastly, Fig. 3c) (top panel) shows the DOS for the carboxyl and lateral chain, where the lateral chain is dominant, with the prevalence of the p orbital for both valence and conduction bands. Additionally, in the valence band, the major contribution is from the linear chain through the C4, C5, and C6, while in the conduction band, there is a mixed contribution of both the carboxyl group through the C1, O1, and O2 atoms and the lateral chain group with the C5, as shown in Fig. 3c) (bottom panel).

We further analyze the electronic results by presenting the effective mass (m^*) of electrons (m_e) in the conduction band and holes (m_h) in the valence band. The inverse of the second derivative of the energy (E) concerning distance in reciprocal space (k) is proportional to m_e and m_h, respectively. The following equation can express these values [45, 48]:

$$\frac{1}{m^*} = \frac{1}{\hbar^2}\frac{\partial^2 E}{\partial k^2}, \tag{1}$$

where $\hbar$ is the reduced Planck's constant. The band curvature at points of interest in the Brillouin zone was calculated for the mLH crystal by fitting quadratic curves, as shown in

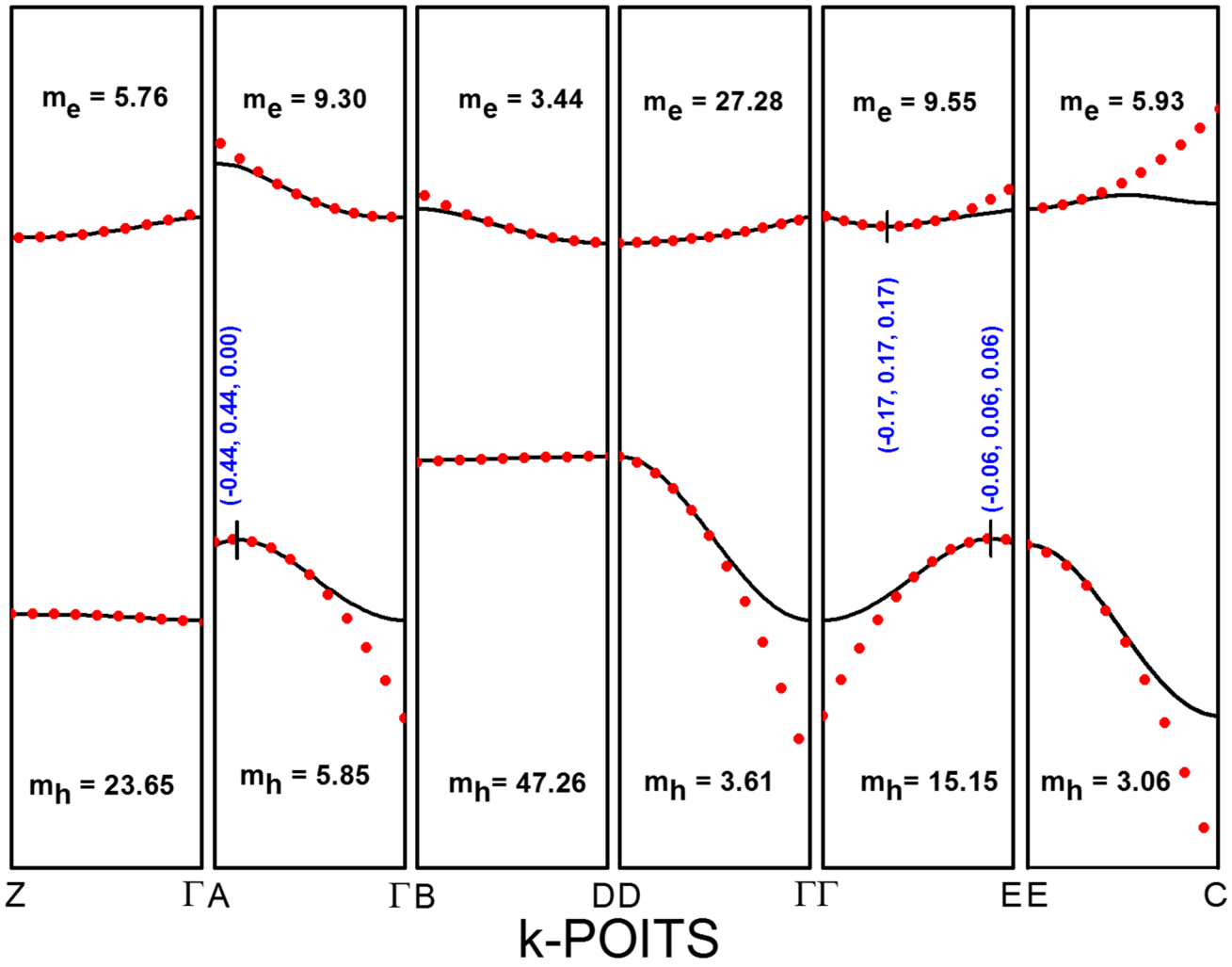

Fig. 4 Energy level fittings to estimate the electron and hole effective masses in mLH crystals

Fig. 4. The effective mass is an important factor in determining the viability of charge transport through the valence and conduction bands. In this way, in Fig. 4, it can be seen that the hole effective masses vary from $3.06m_0$ (at the $E \rightarrow C$ path) to $47.26m_0$ (at the $B \rightarrow D$ path), while the electron masses vary from $3.44m_0$ (at the $B \rightarrow D$ path) to $27.28m_0$ (at the $D \rightarrow \Gamma$ path), where m_0 represents the electron mass.

Figure 5 highlights the valence and conduction bands for special directions, i.e., perpendicular and parallel to the molecular plane of the mLH crystal, indicated by $\perp_D$ and $\|_D$ (refer to Fig. 2). These directions represent the maximum point of the valence band and the minimum point of the conduction band, shown in Fig. 5a) and b) (top panels), respectively. Their related valence and conduction bandwidths (bottom panels) allow evaluation of the effective mass character, with a narrow bandwidth corresponding to a large effective mass and a wide bandwidth to a small effective mass.

In Fig. 5a) (bottom panel), the valence bandwidth reveals that the effective mass for the $\perp_D$ direction (gray bar) is larger than the one for the $\|_D$ direction (black bar). On the other hand, Fig. 5b) (bottom panel) shows that the effective mass for the $\perp_D$ direction (gray bar) is lower than the one for the $\|_D$ direction (black bar) in the conduction band. Moreover, the valence band $\perp_D$ direction has an energy of about 77 meV with $m_h = 3.93m_0$, whereas the $\|_D$ direction presents an energy of about 28 meV with $m_h = 15.33m_0$. Regarding the conduction band and $\perp_D$, the energy is about 29 meV with $m_e = 7.53m_0$, while for the $\|_D$ direction, the energy is about 78 meV with $m_e = 4.16m_0$. It is worth emphasizing that the directions with the lowest effective mass values are more favorable for electronic transference.

Now, we analyzed the partial density of states (PDOS) per atom and functional group. Figure 6a) shows the relative contributions of each atomic species C, O, N, and H. We found that the C, O, and N atoms contribute significantly with p orbitals close to the bandgap for both the valence and conduction bands, whereas the H atom contributes only with s orbitals. Figure 6b) displays the electronic contribution of the carboxyl, amino, imidazole ring, and lateral chain functional groups. We observed that s and p orbitals contribute to both functional groups, with the p orbitals being more prevalent near the valence and conduction bands for the carboxyl, imidazole ring, and lateral chain.

The s orbital contributes prominently only to the most negative energy range of the conduction band in the energy range from -21.25 eV to -11.25 eV for all functional groups constituting the mLH crystal. The amino group has the lowest contribution at the valence and conduction bands. For this group, the s and p orbitals overlap in the vicinity of both bands with PDOS peaks at about 0; electron/eV. On the other hand, the imidazole ring and lateral chain groups

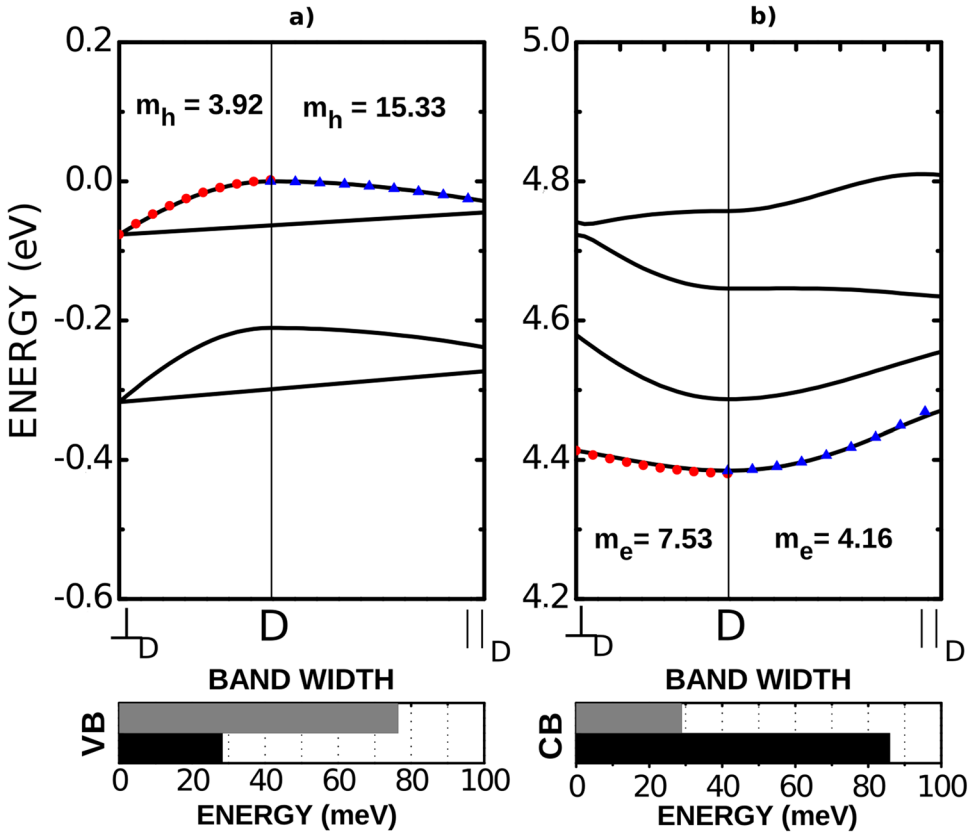

Fig. 5 Top panels show the (a) valence and (b) conduction bands for special directions, i.e., perpendicular and parallel to the molecular plane of the mLH crystal, indicated by $\perp_D$ and $\|_D$ (refer to Fig. 2). The bottom panels depict the related valence and conduction bandwidths

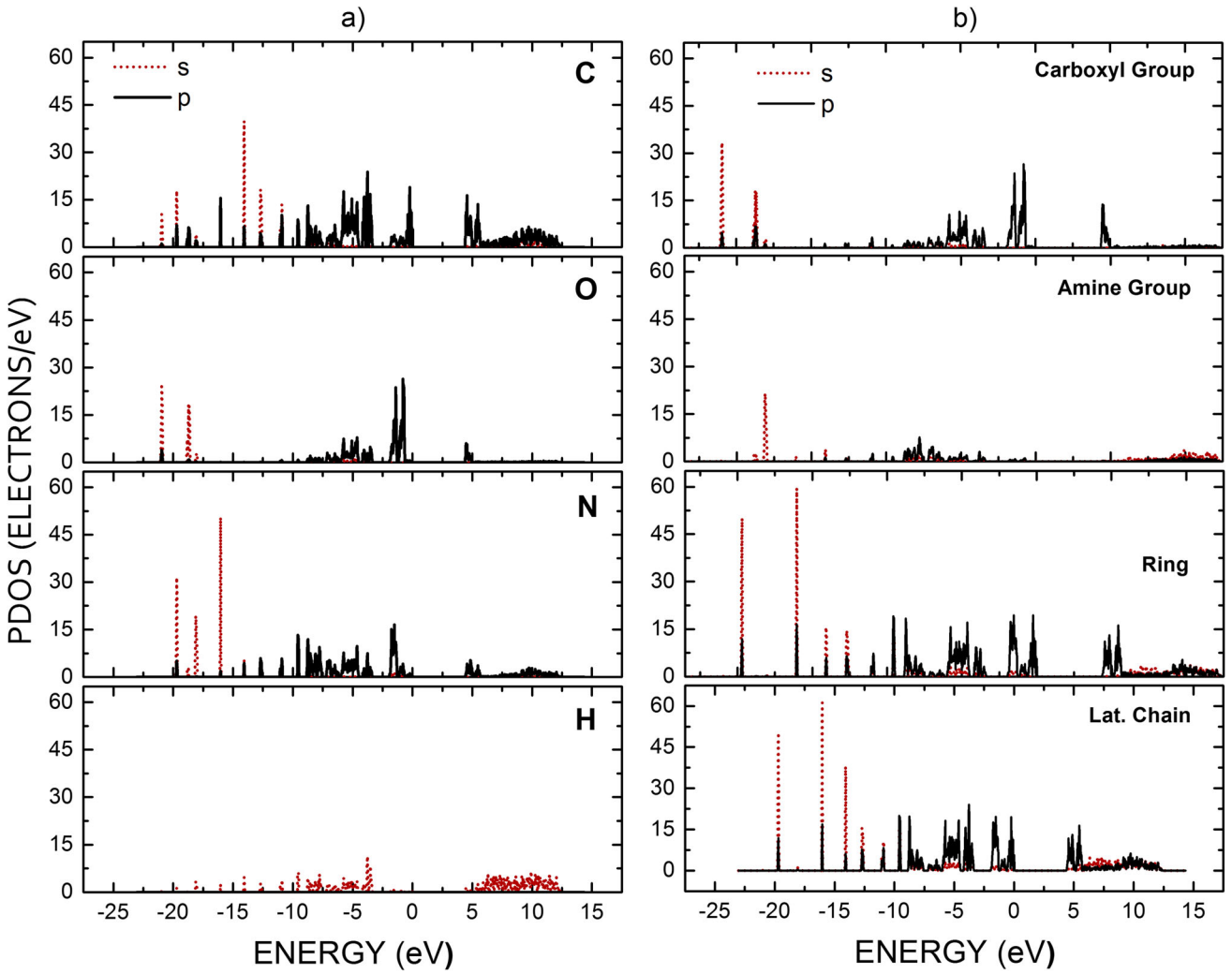

Fig. 6 Partial density of states (PDOS) a) per atom and b) functional groups

present prominent peaks at the valence and conduction bands, differing from the carboxyl group in the same region. This PDOS analysis sheds light on the origin of the relevance of the band structure features of the mLH crystal.

Optical properties

Here, we discuss the optical properties of the mLH crystals. We consider the incident light polarized along the (001), (010), (100), (512) and (10$\bar{5}$) directions, as well as one polycrystalline sample. The incident light planes (512) and (10$\bar{5}$) correspond to the $\perp_D$ and $\|_D$ special directions (refer to Fig. 2).

Figure 7 shows the optical absorption behavior of the mLH crystal when the incident light is polarized along the selected crystal planes mentioned earlier. The absorption spectrum varies in the energy range of approximately 4.0 eV to 24.0 eV, indicating an intense optical absorption activity in the ultraviolet region (UV). This absorption range is important for optoelectronic devices that act as UV collectors.

Notably, a prominent peak of light absorption is observed in the (001), (100), (512), and (10$\bar{5}$) directions at about 4.0 eV to 10.0 eV, with emphasis on the (001) direction. The (010) direction shows low optical absorption activity in the same range. The energy range from about 10.0 eV to 24.0 eV shows the region of the greatest absorption, with peak absorption around 16.0 eV. The mLH crystal exhibits anisotropic behavior, except for the (512) and (10$\bar{5}$) directions. Moreover, the polycrystalline sample shows the typical overall behavior of optical absorption seen in the (001), (100), (512), and (10$\bar{5}$) directions.

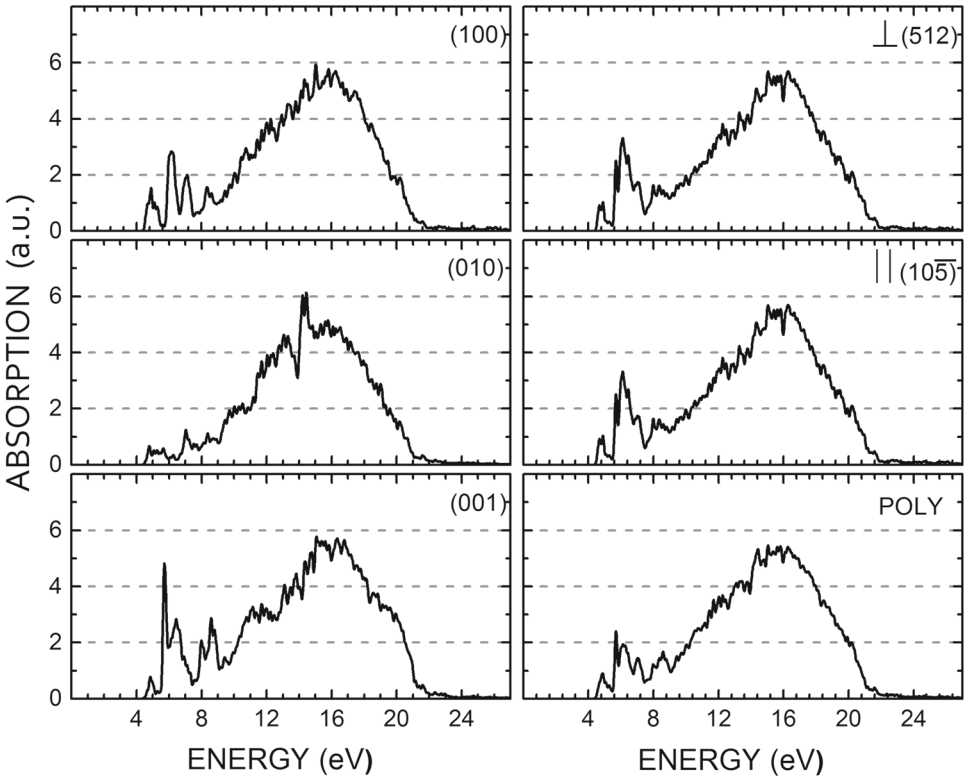

Fig. 7 Optical absorption of mLH crystal along the (001), (010), (100), (512) and (10$\bar{5}$) incidence directions. The optical absorption for a polycrystalline sample is also shown

Finally, Fig. 8 displays the real (black) and imaginary (red) parts of the dielectric function of the photon energy. The dielectric function exhibits an anisotropic behavior along the incident planes, except for the (001) and (10$\bar{5}$) directions, which have the same behavior. The (001) and (10$\bar{5}$) directions have the most significant peaks in terms of amplitude for the (001), (100), (512), and (10$\bar{5}$) directions. The (010) direction has no peak in the same region. Furthermore, the amplitude of the real and imaginary parts of the dielectric function varies, indicating the presence of a strong dipole moment induced by the electric field of the incident light. The dielectric function of the polycrystalline sample shows the typical overall behavior for (001), (100), (512), and (10$\bar{5}$) directions.

The amplitude of the real and imaginary parts of the dielectric function varies due to a strong dipole moment induced by the light [62]. Light interacting with material creates a polarization effect that moves electrons and generates a dipole moment [63]. This dipole moment interacts with the light's electromagnetic field and is reflected in the dielectric function [63]. The real part of the dielectric function represents the material's ability to store electrical energy, while the imaginary part represents its ability to dissipate electrical energy [64]. The variation in the amplitude of these two parts shows that the material responds differently to the electric field of the light due to the dipole moment induced by the light [64]. Thus, the strength of the induced dipole moment affects the amplitude of the real and imaginary parts of the dielectric function.

Conclusions

In summary, we have investigated the optical properties of mLH using first-principles calculations. Our results showed that our calculated structural properties matched well with experimental findings. The electronic band structure revealed that mLH is an insulator material with a direct band gap of about 4.38 eV. Furthermore, effective mass calculations indicated the possibility of charge transport through valence and conduction bands, especially along directions with the lowest effective mass values. The hole effective masses vary from $3.06m_0$ to $47.26m_0$, while the electron masses vary from $3.44m_0$ to $27.28m_0$.

The mLH crystal exhibits anisotropic behavior in optical absorption and dielectric function along different incident planes. The absorption spectrum varies in the energy range of approximately 4.0 eV to 24.0 eV, indicating an intense optical absorption activity in the ultraviolet region (UV). This absorption range is important for optoelectronic devices that act as UV collectors.

Generally, it is difficult to directly compare the optical response of L-histidine with other dyes or materials due to the differences in their molecular structures and electronic prop-

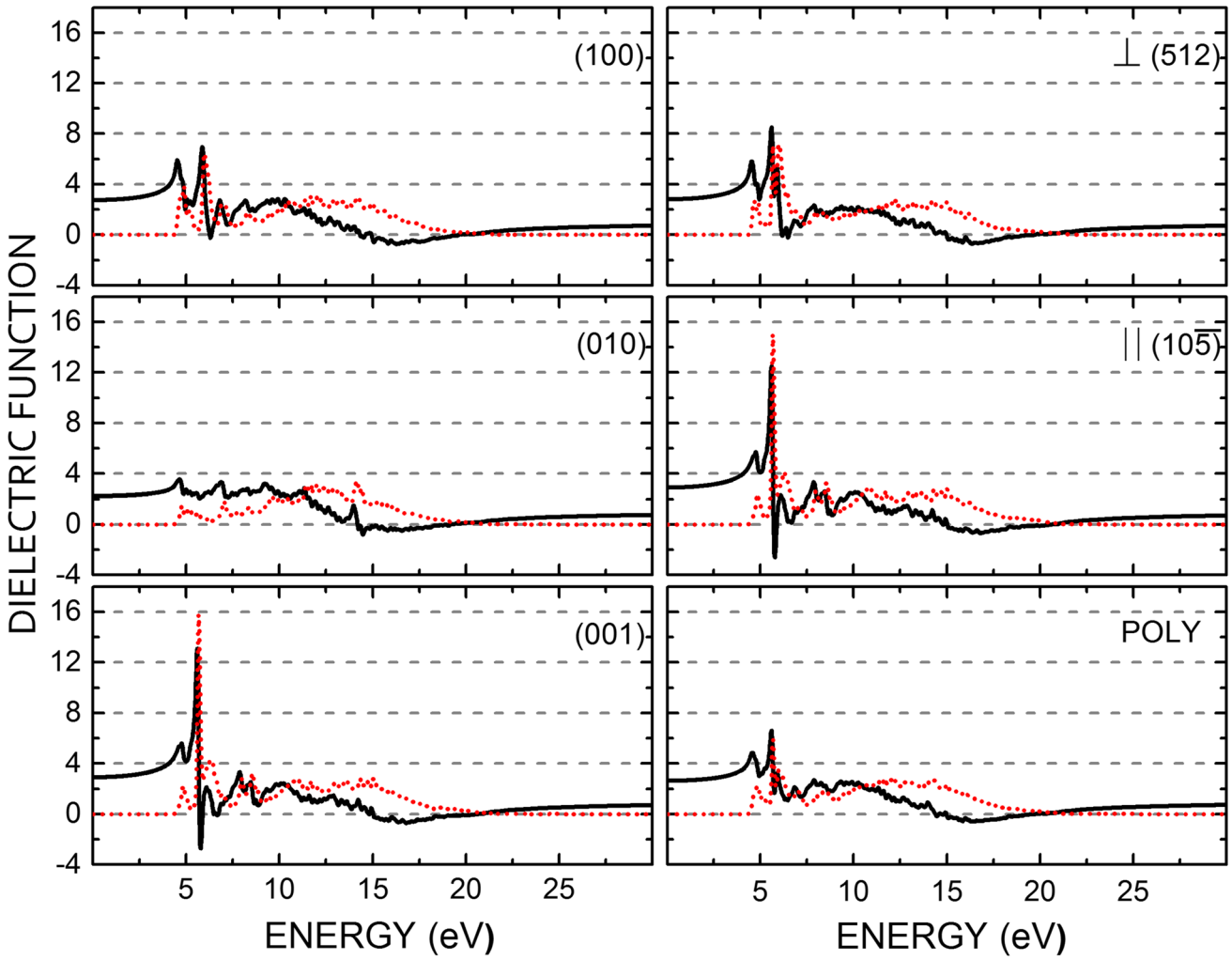

Fig. 8 Real (black) and imaginary (red) parts of the dielectric function for mLH crystal along the (001), (010), (100), (512) and (10$\bar{5}$) incidence directions. The same quantities are also illustrated for the polycrystalline

erties. The relevance of the optical response of L-histidine depends on the specific application and the device's requirements. For example, if a device needs to detect UV light in a specific range, the absorption spectrum of L-histidine in that range would be compared to that of other materials to determine its effectiveness. L-Histidine's cost, stability, and availability should also be considered when its performance is compared to other materials.

Acknowledgements We acknowledge the Laboratório de Física Teórica e Modelagem Computacional (LFTMC), Teresina-PI, Brazil, and the Cluster Saturno, Fortaleza-CE, Brazil, for providing the computational facilities. L.A.R.J acknowledges the financial support from Brazilian Research Council FAP-DF grants 00193 − 00001247/2021 − 20, 00193 − 00000811/2021 − 97, 00193.00001808/2022 − 71, and 00193 − 00000857/2021 − 14, CNPq grants 302236/2018 − 0 and 350176/2022 − 1, and FAPDF-PRONEM grant 00193.00001247/2021 −20. This study was financed in part by the Coordenação de Aperfeiçoamento de Pessoal de Nível Superior - Brasil (CAPES) - Finance Code 88887.691997/2022-00. L.A.R.J. gratefully acknowledges the support from ABIN grant 08/2019. A.M.F. gratefully acknowledges the support from Conselho Nacional de Desenvolvimento Científico (CNPq), grants 459961/2014 − 4 and 424950/2018 − 9.

Author contribution F.A.R.P, A.M.S., N.F.F., R.G.S., and K.A.L.L.: data curation, formal analysis, methodology, and writing — original draft preparation. J.J.S.M., M.L.P.J, and A.M.F.: data curation, formal analysis, methodology, and funding acquisition. L.A.R.J. and V.N.F.: conceptualization, funding acquisition, and writing — reviewing and editing. All authors reviewed the manuscript.

Funding Brazilian Research Councils FAP-DF, CNPq, and CAPES.

Code availability N/A

Declarations

Conflict of interest The authors declare no competing interests.

References

1. Kulis-Horn RK, Persicke M, Kalinowski J (2014) Histidine biosynthesis, its regulation and biotechnological application in Corynebacterium glutamicum. Microb Biotechnol 7:5–25
2. Krajewska-Grynkiewicz K, Walczak W, Kłopotowski T (1971) Mutants of Salmonella typhimurium Able to Utilize d-Histidine as a Source of L-Histidine. J Bacteriol 105:28–37
3. Faria JLB et al (2004) Raman spectra of L-histidine hydrochloride monohydrate crystal. J Raman Spectrosc 35:242–248
4. Ingle RA (2011) Histidine biosynthesis. Arabidopsis Book 9:1543–8120
5. Nelson DL, Cox MM (2004) Lehninger Principles of Biochemistry, 4th edn. Worth Publishers, New York
6. Wang Y, Zhao Z, Qin J, Liu H, Liu A, Xu M (2020) Rapid in situ analysis of L-histidine and α-lactose in dietary supplements by fingerprint peaks using terahertz frequency-domain spectroscop. Talanta 208:120469
7. Amir R, Galili G, Cohen H (2018) The metabolic roles of free amino acids during seed development. Plant Sci 275:11–18
8. Watford M, Wu G (2018) Protein. Adv Nutr 9:651–653
9. Perez-Benito JF, Julian-Millan X (2019) Ligand substitution in chromium(III)-aqua complexes by l-histidine: kinetic resolution of two long-lived intermediates. React Kinet Mech Catal 128:1–22
10. Murray RK, Granner DK, Mayer PA, Rodwell VW (2003) Harper's Illustrated Biochemistry, 26th edn. McGraw-Hill Medical, New York
11. Holecek M (2020) Histidine in Health and Disease: Metabolism, Physiological Importance, and Use as a Supplement. Nutrients 12:848
12. Hecel A, Wątly J, Rowinska-Zyrek M, Swiątek-Kozlowska J, Kozlowski H (2018) Histidine tracts in human transcription factors: insight into metal ion coordination ability. J Biol Inorg Chem 23:81–90
13. Iswarya CN, Kiruba Daniel SCG, Sivakumar M (2017) Studies on L-histidine capped Ag and Au nanoparticles for dopamine detection. Mater Sci Eng C75:393–401
14. Liao S, Du Q, Meng J, Pang Z, Huang R (2013) The multiple roles of histidine in protein interactions. Chem Cent J 7:44
15. Xu L, Li Y, Zhou Q, Deng X (2020) A comparative study of the low-frequency vibrations of L-histidine molecule in different solid states. Spectrochim Acta A Mol Biomol Spectrosc 224:117468
16. John NL, Abraham S, Sajan D, Philip R, Joy N, Chitra R (2020) Molecular structure, NLO properties and vibrational analysis of L-Histidine tetra fluro borate by experimental and computational spectroscopic techniques. Spectrochim Acta A Mol Biomol Spectrosc 226:117615
17. Sagadevan S, Varatharajan R (2013) Technological Importance of L-histidine Family of NLO Single Crystals. Mater Phys Mech 18:11–17
18. Suresh AS, Ramanand A, Jayaraman D, Mani P (2012) Review on Theoretical Aspect of Nonlinear Optics. Rev Adv Mater Sci 30:175–183
19. Ahmed B, Feki H, Abid Y, Boughzala H, Mlayah A (2008) Structural, vibrational and theoretical studies of L-histidine bromide. J Mol Struct 888:180–186
20. Fleck M, Ghazaryan VV, Bezhanova LS, Atanesyan AK, Petrosyan AM (2013) New crystals of L-histidine maleates. J Mol Struct 1035:407–415
21. Vinayagamoorthy R, Irudayaraj AA, Raj AD, Karthick S, Jayakumar G (2017) Comparative Study of Properties of L-Histidine and L-Histidine Nickel Nitrate Hexahydrate CrystalsGrown by Slow Evaporation. Mech Mater Sci Eng J Magnolithe 9. https://doi.org/10.2412/mmse.83.74.689. hal-01503639
22. Nalini H, Vincent VC, Bakiyaraj G, Kirubavathi K, Selvaraju K (2020) Structural, optical, laser damage, NLO and theoretical analysis of L-histidine L-aspartate monohydrate crystals. Phys B Phys Condens Matter 592:412245
23. Revathi V, Karthik K (2018) Growth, spectral, optical, thermal, electrical, mechanical and etching studies of organic single crystal: l-histidinium l-tartrate hemihydrate. J Mater Sci Mater Electron 29:17323–17332
24. Misoguti L, Varela AT, Nunes FD, Bagnato VS, Melo FEA, Mendes Filho J, Zilio SC (1996) Optica properties of L-alanine organic crystals. Opt Mater 6:147–152
25. Kumar GR, Raj SG, Mohan R, Jayavel R (2005) Growth, structual ans spectral analyses of nonlinear optical L-threonine single crystal. J Cryst Growth 275:e1947–e1951
26. Muley GG, Ambhore PS, Naik AB, Gambhire AB (2016) Effect of partial replacement of Zn with Cd on optical properties of zinc thiourea chloride (ZTC) crystal. Procedia Technol 24:715–720
27. Koteeswari P, Suresh S, Mani P (2012) Crystal grwoth, optical and dieletric properties of L-histidine hydrocloride monohydrate nonlinear optical single crystal. J Mater Charact Eng 11:813–816
28. Raj PA, Raja CR (2013) Synthesis, growth, structural, spectroscopic, thermal and optical properties of NLO single crystal: L-threonine zinc acetate. Photon Opto Electron 2:56–64
29. Madden JJ, McGandy EL, Seeman NC, Harding MM, Hoy A (1972) The crystal structure of the monoclinic form of L-histidine. Acta Crystallogr Sect B Struct Crystallogr Cryst Chem 28:2382–2389
30. Madden JJ, McGandy EL, Seeman NC (1972) The crystal structure of the ortorhombic form of L-(+)-histidine. Acta Crystallogr Sect B Struct Crystallogr Cryst Chem 28:2377–2382
31. Hohenberg P, Kohn W (1964) Inhomogeneous electron gas. Phys Rev 136:864B
32. Kohn W, Sham LJ (1965) Self-consistent equations including exchange and correlation effects. Phys Rev 140:1133A
33. Santos JGS, Macedo-Filho A, Silva AM, de Sousa FF, Caetano EWS, da Silva MB, Freire VN (2021) Computational structural, electronic and optical properties of the palmitic acid in its C form. J Mol Model 27:145
34. Viana GED, Silva AM, da C Barros FU, da Silva FJAM, Caetano EWS, Melo JJS, Macedo-Filho A, (2020) Thermal stability and electronic properties of boron nitride nanoflakes. J Mol Model 26:100
35. Perdew JP, Burke K, Ernzerhof M (1996) Generalized Gradient Approximation Made Simple. Phys Rev Lett 77:3865
36. Payne MC, Teter MP, Allan DC, Arias TA, Joannopoulos JD (1992) Iterative minimization techniques for ab initio total-energy calculations: molecular dynamics and conjugate gradients. Rev Mod Phys 64:1045
37. Segall D, Lindan PJD, Probert MJ, Pickard CJ, Hasnip PJ, Clark SJ, Payne MC (2002) First-principles simulation: Ideas, illustrations and the castep code. J Phys Condens Matter 14:2717–2744
38. Perdew JP, Wang Y (1992) Accurate and simple analytic representation of the electron-gas correlation energy. Phys Rev B 45:13244–13249
39. Tkatchenko A, Scheffler M (2009) Accurate molecular van der waals interactions from ground-state electron density and free-atom reference data. Phys Rev Lett 102:073005
40. Madden JJ, McGandy EL, Seeman NC, Harding MM, Hoy A (1972) The crystal structure of the monoclinic form of l-histidine. Acta Cryst B28:2382–2389
41. Lin JS, Qteish A, Payne MC, Heine V (1993) Optimized and transferable non local separable ab initio pseudopotentials. Phys Rev B 47:4174–4180

42. Pfrommer BG, Cote M, Louie SG, Cohen ML (1997) Relaxation of crystals with the quasi-newton method. J Comput Phys 131:233–240
43. Mulliken RS (1955) Electronic Population Analysis on LCAO-MO Molecular Wave Functions. I J Chem Phys 23:1833–1840
44. Hirshfeld FL (1977) Bonded-atom fragments for describing molecular charge densities. Theor Chim Acta 44:129–138
45. Silva AM, Silva BP, Sales FAM, Freire VN, Moreira E, Fulco UL, Albuquerque EL, Maia FF Jr, Caetano EWS (2012) Optical absorption and DFT calculations in L-aspartic acid anhydrous crystals: Charge carrier effective masses point to semiconducting behavior. Phys Rev B 86:195201
46. Koerner MM, Palacio LA, Wright JW, Schweitzer KS, Ray BD, Petrache HI (2011) Electrodynamics of Lipid Membrane Interactions in the Presence of Zwitterionic Buffers. Biophys J. 101:362–369
47. Qian L, Liu W, Yang M, Nica V, Yang J, Liu H, Ning L, Zhang S, Zhang Q (2020) Zwitterionic polymer chain-assisted lysozyme imprinted core-shell carbon microspheres with enhanced recognition and selectivity. Talanta 217:121085
48. Liu WH, Zeng W, Liu FS, Tang B, Liu QJ (2020) Electronic properties and effective masses of hexagonal Bi9O7.5S6: first-principles calculations. Mater Sci Semicond Process 114:105081
49. Hareter A, Hoffmann E, Bode HP, Göke B, Göke R (1997) The Positive of the Imidazole side Chain of Histidine7 Is Crucial for GLP-1 Action. Endocr J 44:701–705
50. Roth A, Breaker RR (1998) An amino acid as a cofactor for a catalytic polynucleotide. Proc Natl Acad Sci 95(11):6027–6031
51. Del Carpio E, Hernández L, Ciangherotti C, Coa VV, Jiménez L, Lubes V, Lubes G (2018) Vanadium: History, chemistry, interactions with α-amino acids and potential therapeutic applications. Coord Chem Rev 372:117–140
52. Baslé E, Joubert N, Pucheault M (2010) Protein chemical modification on endogenous amino acids. Chem Biol 17(3):213–227
53. Wade AM, Tucker HN (1998) Antioxidant characteristics of L-histidine. J Nutr Biochem 9(6):308–315
54. Ercan-Sencicek AG, Stillman AA, Ghosh AK, Bilguvar K, O'Roak BJ, Mason CE, State MW (2010) L-histidine decarboxylase and Tourette's syndrome. N Engl J Med 362(20):1901–1908
55. Aggarwal MD, Choi J, Wang WS, Bhat K, Lal RB, Shields AD, Frazier DO (1999) Solution growth of a novel nonlinear optical material: L-histidine tetrafluoroborate. J Cryst Growth 204(1–2):179–182
56. Petrosyan HA, Karapetyan HA, Petrosyan AM (2006) L-Histidine nitrates. J Mol Struct 794(1–3):160–167
57. Madden JJ, McGandy EL, Seeman NC, Harding MM, Hoy A (1972) The crystal structure of the monoclinic form of L-histidine. Acta Crystallogr B Struct Crystallogr Cryst Chem 28(8):2382–2389
58. Tiwari OS, Aizen R, Meli M, Colombo G, Shimon LJ, Tal N, Gazit E (2023) Entropically-Driven Co-assembly of l-Histidine and l-Phenylalanine to Form Supramolecular Materials. ACS Nano 17(4):3506–3517
59. Sweatha L, Sivakumar A, Martin Britto Dhas SA, Silviya M, Anithalakshmi M, Robert R (2023) Investigations on structural and optical properties of L-histidine hydrochloride monohydrate crystals at dynamic shock wave-loaded conditions. J Mater Sci Mater Electron 34(5):419
60. Riffet V, Bouchoux G (2013) Gas-phase structures and thermochemistry of neutral histidine and its conjugated acid and base. Phys Chem Chem Phys 15:6097–6106
61. Lee SS, Kim JY, Han Y, Shim HJ, Lee S (2015) Thermodynamic and kinetic stability of zwitterionic histidine: Effects of gas phase hydration. Chem Phys Lett 637:42–50
62. Loudon R (1970) The propagation of electromagnetic energy through an absorbing dielectric. J Phys A Gen Phys 3:233
63. Glass AM, Von der Linde D, Auston DH, Negran TJ (1975) Excited state polarization, bulk photovoltaic effect and the photorefractive effect in electrically polarized media. J Electron Mater 4:915–943
64. Liang C, Sun FP, Rogers CA (1997) Coupled electro-mechanical analysis of adaptive material systems-determination of the actuator power consumption and system energy transfer. J Intell Mater Syst Struct 8(4):335–343

Authors and Affiliations

F. A. R. Pereira[1] · A. Macedo-Filho[1,2] · A. M. Silva[3] · N. F. Frazão[4] · R. G. Sarmento[5] · K. A. L. Lima[1] · J. J. S. Melo[6] · M. L. Pereira Junior[7] · L. A. Ribeiro Junior[8] · V. N. Freire[9]

1 PPGQ-GERATEC, State University of Piauí, 64002-150 Teresina, PI, Brazil

2 Department of Physics, State University of Piauí, 64002-150 Teresina, PI, Brazil

3 Campus Prof. Antonio Geovanne Alves de Sousa, State University of Piauí, 64260-000 Piripiri, PI, Brazil

4 Center for Education and Health, Federal University of Campina Grande, 581750-000 Cuité, PB, Brazil

5 Campus Minister Petrônio Portella, Federal University of Piauí, 64049-550 Teresina, PI, Brazil

6 Department of Physics, Federal Institute of Maranhão, Monte Castelo Campus, 65030-005 São Luis, MA, Brazil

7 Department of Electrical Engineering, Faculty of Technology, University of Brasília, 70910-900 Brasília, Brazil

8 Institute of Physics, University of Brasilia, 70910-900 Brasília, Brazil

9 Department of Physics, Federal University of Ceará, 60455-760 Fortaleza, CE, Brazil